Supplementary Materials - Vulnerability of firn to hydrofracture: poromechanics modeling

Yue Meng[1,3*], Riley Culberg[2,3*], and Ching-Yao Lai[1,3]

[1]Department of Geophysics, Stanford University, Stanford, CA, USA
[2]Department of Earth and Atmospheric Sciences, Cornell University, Ithaca, NY, USA
[3]Department of Geosciences, Princeton University, Princeton, NJ, USA

May 23, 2024

* Corresponding author: olivmeng@stanford.edu, rtc84@cornell.edu

1 The poroelastic and analytical models

Details of algebra of Eqn. 16 in the main text

Combining Eqn. 12 and Eqn. 15 in the main text, we expand equation Eqn. 11 in the main text as follows:

$$
\begin{aligned}
\frac{\partial(\phi\rho_\alpha S_\alpha)}{\partial t} + \nabla\cdot(\rho_\alpha\phi S_\alpha \boldsymbol{v_\alpha}) &= 0,\\
\Rightarrow \phi\frac{\partial(\rho_\alpha S_\alpha)}{\partial t} + \rho_\alpha S_\alpha\frac{\partial\phi}{\partial t} + \nabla\cdot(\rho_\alpha \boldsymbol{q}_\alpha + \rho_\alpha\phi S_\alpha \boldsymbol{v}_s) &= 0,\\
\Rightarrow \phi\rho_\alpha\frac{\partial S_\alpha}{\partial t} + \phi S_\alpha\frac{\partial\rho_\alpha}{\partial t} + \rho_\alpha S_\alpha\frac{\partial\phi}{\partial t} + \nabla\cdot(\rho_\alpha\boldsymbol{q}_\alpha)&\\
+\rho_\alpha\phi S_\alpha\nabla\cdot\boldsymbol{v}_s + \boldsymbol{v}_s\cdot\nabla(\rho_\alpha\phi S_\alpha) &= 0,\\
\Rightarrow \phi\rho_\alpha\frac{\partial S_\alpha}{\partial t} + \phi S_\alpha\rho_\alpha\frac{1}{\rho_\alpha}\frac{\partial\rho_\alpha}{\partial(\delta p)}\frac{\partial(\delta p)}{\partial t} + \rho_\alpha S_\alpha\frac{\partial\phi}{\partial t} + \nabla\cdot(\rho_\alpha\boldsymbol{q}_\alpha)&\\
+\rho_\alpha\phi S_\alpha\frac{\partial(\delta\epsilon_{kk})}{\partial t} + \boldsymbol{v}_s\cdot\nabla(\rho_\alpha\phi S_\alpha) &= 0,\\
\Rightarrow \phi\rho_\alpha\frac{\partial S_\alpha}{\partial t} + \phi S_\alpha\rho_\alpha c_\alpha\frac{\partial(\delta p)}{\partial t} + \rho_\alpha S_\alpha(b-\phi)(c_s\frac{\partial(\delta p)}{\partial t} + \frac{\partial(\delta\epsilon_{kk})}{\partial t}) + \nabla\cdot(\rho_\alpha\boldsymbol{q}_\alpha)&\\
+\rho_\alpha\phi S_\alpha\frac{\partial(\delta\epsilon_{kk})}{\partial t} + \boldsymbol{v}_s\cdot\nabla(\rho_\alpha\phi S_\alpha) &= 0,\\
\Rightarrow \phi\rho_\alpha\frac{\partial S_\alpha}{\partial t} + \rho_\alpha S_\alpha\left(b\frac{\partial(\delta\epsilon_{kk})}{\partial t} + (\phi c_\alpha + (b-\phi)c_s)\frac{\partial(\delta p)}{\partial t}\right) + \nabla\cdot(\rho_\alpha\boldsymbol{q}_\alpha) + \boldsymbol{v}_s\cdot\nabla(\rho_\alpha\phi S_\alpha) &= 0,
\end{aligned}
\tag{S1}
$$

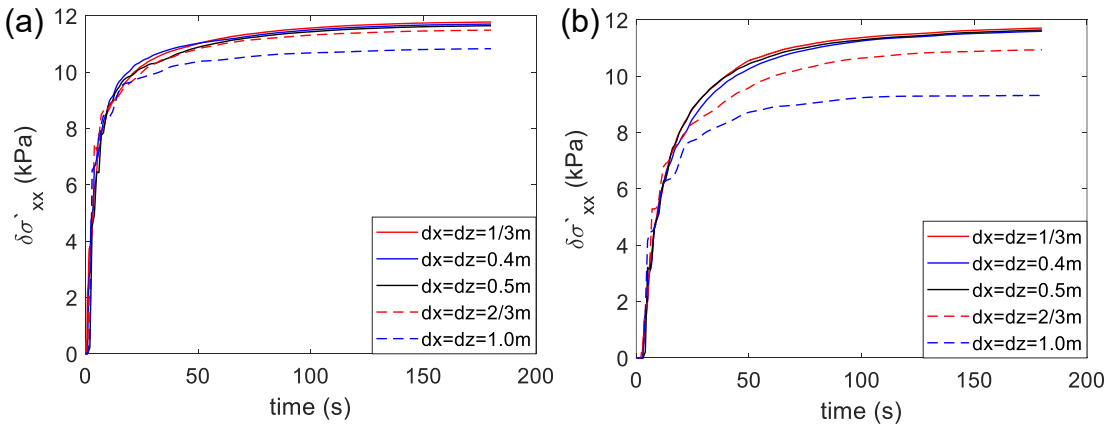

Figure S1: Convergence and mesh independence analysis. Time evolution of the infiltration-induced horizontal effective stress change at the crevasse tip $\delta\sigma'_{xx}(t)$ for (a) $H_w = 10$ m, (b) $V_{\text{inj}} = 0.05$ m s^{-1}, with a decreasing mesh size from 1 m (900 elements in the domain) to 1/3 m (8100 elements in the domain). The modeling results converge at a mesh size of 0.5 m, which is adopted for all the simulation presented in this paper.

where c_α (Pa^{-1}) is the compressibility of fluid phase obtained from the equation of state (for isothermal conditions and immiscible phases):

$$c_\alpha = \frac{1}{\rho_\alpha}\frac{\partial \rho_\alpha}{\partial p_\alpha}. \tag{S2}$$

$\boldsymbol{v_s}$, $\delta\epsilon_{kk}$ are the infiltration-induced velocity and the volumetric strain of the solid phase, respectively. The rate of change of volumetric strain $\delta\epsilon_{kk}$ can be expressed as $\frac{\partial(\delta\epsilon_{kk})}{\partial t} = \nabla \cdot \boldsymbol{v}_s$.

We make several assumptions to simplify Eqn. (S1). We first drop the last term, $\boldsymbol{v}_s \cdot \nabla(\rho_\alpha \phi S_\alpha)$, which has negligible effects on the flow equation when injecting fluid into geologic formation (Bjørnarå and others, 2016; Meng and others, 2023). The two phase fluids in the model (water and air) are immiscible, which simplifies the phase behavior of the system (Jha and Juanes, 2014). For the air phase, the density does not change in the dry, porous firn. For the water phase, the density variation under the imposed pressure range ($\sim$ 100 kPa) is smaller than 0.005%. Therefore, we assume constant densities for both fluid phases and the density (ρ_α) comes out of the divergence. We arrive at the final expression for fluid flow equations as follows (Eqn. 16 in the main text):

$$\phi\frac{\partial S_\alpha}{\partial t} + S_\alpha\left(b\frac{\partial(\delta\epsilon_{kk})}{\partial t} + (\phi c_\alpha + (b-\phi)c_s)\frac{\partial(\delta p)}{\partial t}\right) + \nabla \cdot \boldsymbol{q}_\alpha = 0. \tag{S3}$$

Convergence and mesh independence analysis

Figure S1 shows the time evolution of infiltration-induced horizontal effective stress change at the crevasse tip ($\delta\sigma'_{xx,\max}(t)$) under constant pressure and injection velocity conditions. The mesh size decreases from 1 m (900 elements in the domain) to 1/3 m (8100 elements in the domain). The modeling results converge at a mesh size of 0.5 m, which is adopted for all the simulation presented in this paper.

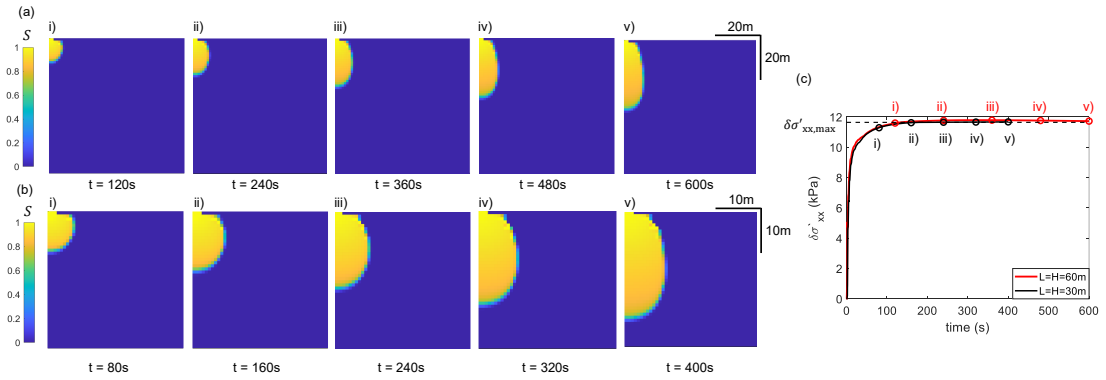

Figure S2: Modeling results for the water infiltration with $H_w = 10$ m in the domain $0 < x < L$, $0 < z < H$. A sequence of snapshots shows the spatiotemporal evolution of the water saturation field, $S_w(x, z, t)$, for (a) $L = H = 60$ m. The simulation ends when the infiltration front reaches half of the domain size. (b) $L = H = 30$ m and simulation ends when the infiltration front reaches $\frac{4}{5}$ of the domain size. (c) Time evolution of infiltration-induced horizontal effective stress change at the crevasse tip $\delta\sigma'_{xx}(t)$, for two different domain sizes ($L = H = 30$ or 60 m). The markers indicate times for the snapshots shown in (a) and (b).

Modeling results with longer simulation time

In the main text, we have derived a depth value, H_0, below which the infiltration becomes purely gravity-driven and makes no impact on the pore pressure or effective stress. Therefore, the effective stress increases until the infiltration front reaches H_0, and then stays in a plateau afterwards. For all the simulations presented in Figure 5 in the main text, we calculate that H_0 ranges from 2.1 m $\sim$ 9.8 m. As we terminate the simulation when the infiltration front reaches a depth of 15 m, the effective stress is expected to have already reached its maximum value by then. To confirm that the effective stress value ($\delta\sigma'_{xx,max}$) we used in the analysis reaches the maximum during the infiltration, we conduct two separate simulations with longer simulation time. In the first simulation, we use a domain size twice as large as in simulations in the main text, and terminate the simulation when the infiltration front reaches half of the domain size. In the second simulation, we use the same domain size as in the main text, but terminate the simulation when the infiltration front reaches $\frac{4}{5}$ the domain size. The results are presented in Figure S2. After t=160 s, the infiltration is mainly gravity-driven, as evidenced by the fixed horizontal extent and downward motion of the infiltration front in Figure S2(a)(b). The effective stress also reaches a plateau around $t = 200$ s (Fig. S2(c)). The dashed black line shows the effective stress value we used for the analysis in the main text, which effectively captures the maximum effective stress developed during the infiltration. We find that the increase in $\delta\sigma'_{xx,max}$ by extending simulation time is around 0.03 kPa, which increases the fitted parameter β from 0.2166 to 0.2169.

Scaling between $\delta\sigma'_{xx,\mathbf{max}}$ and δp under large $V_{\mathbf{inj}}$ or $L_{\mathbf{crev}}$

For constant injection velocity cases with an unrealistically large crevasse opening or water injection velocity at the crevasse tip, the invading front keeps expanding in a quarter circular-like shape, and H_0 is replaced by the water depth when we terminate the simulation. We

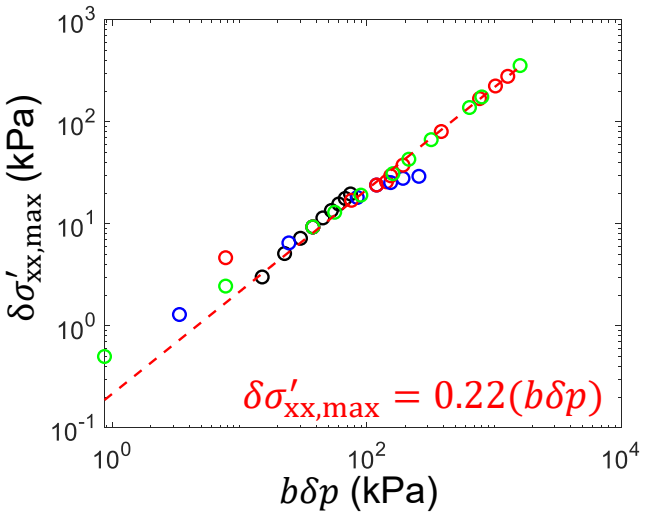

Figure S3: The scaling between $\delta\sigma'_{\mathrm{xx,max}}$ and $b\delta p$. Markers represent all simulation data from water infiltration with a constant injection velocity. The dashed red line represents the analytical prediction: $\delta\sigma'_{\mathrm{xx,max}} = \beta\delta p$, with the prefactor $\beta = 0.22$.

incorporate this scenario into the expression of δp as follows:

$$\delta p = \begin{cases} \frac{5}{3\pi}\frac{\eta_w V_{\mathrm{inj}} L_{\mathrm{crev}}}{k_0} ln(\frac{\eta_w V_{\mathrm{inj}}}{\rho_w g k_0}), \text{ if } \quad V(\alpha H) \leq V_{\mathrm{grav}}, \\ \frac{5}{3\pi}\frac{\eta_w V_{\mathrm{inj}} L_{\mathrm{crev}}}{k_0} ln(1 + \frac{\pi\alpha H}{2L_{\mathrm{crev}}}), \text{ if } \quad V(\alpha H) > V_{\mathrm{grav}}, \end{cases} \tag{S4}$$

where αH is the depth at which we terminate the simulation, and $\alpha = 0.5$ in this paper. The constant injection velocity simulation results for a range of $b, V_{inj}, L_{crev}, k_0$ (unrealistically large V_{inj} or L_{crev}) agrees well with our proposed scaling $\delta\sigma'_{xx,\mathrm{max}} = 0.22(b\delta p)$ as shown in Figure S3. This agreement serves as an additional validation of our numerical simulation, and demonstrates the universality of the scaling relationship $\delta\sigma'_{xx,\mathrm{max}} = 0.22(b\delta p)$.

2 Applications to the Greenland ice sheet

Supplementary Figures S4 and S5 show the laboratory and field measurements used to develop the relations between firn density and firn mechanical properties that are given in Table 2 in the main text.

References

Bjørnarå TI, Nordbotten JM and Park J (2016) Vertically integrated models for coupled two-phase flow and geomechanics in porous media. *Water Resources Research*, **52**(2), 1398–1417 (doi: 10.1002/2015WR017290)

Jha B and Juanes R (2014) Coupled multiphase flow and poromechanics: A computational model of pore pressure effects on fault slip and earthquake triggering. *Water Resources Research*, **50**(5), 3776–3808 (doi: 10.1002/2013WR015175)

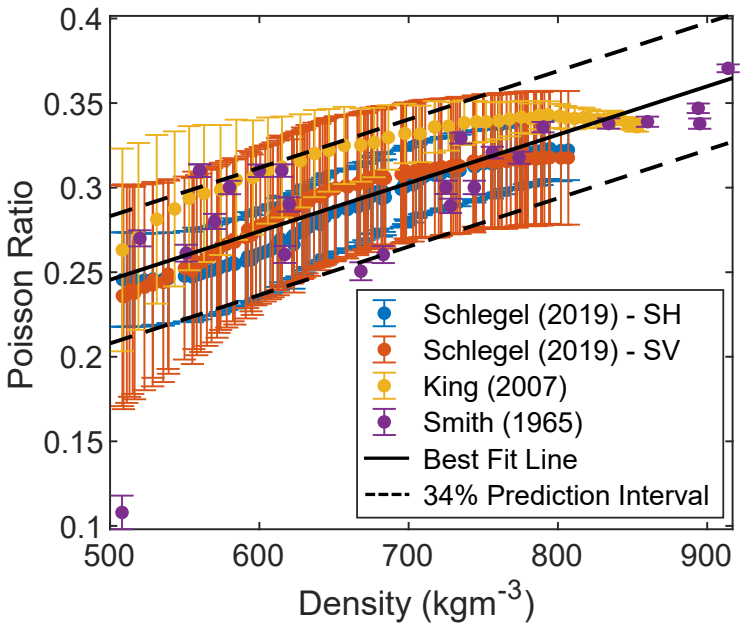

Figure S4: Data points and best fit line approximating the relationship between firn density and the Poisson Ratio of firn.

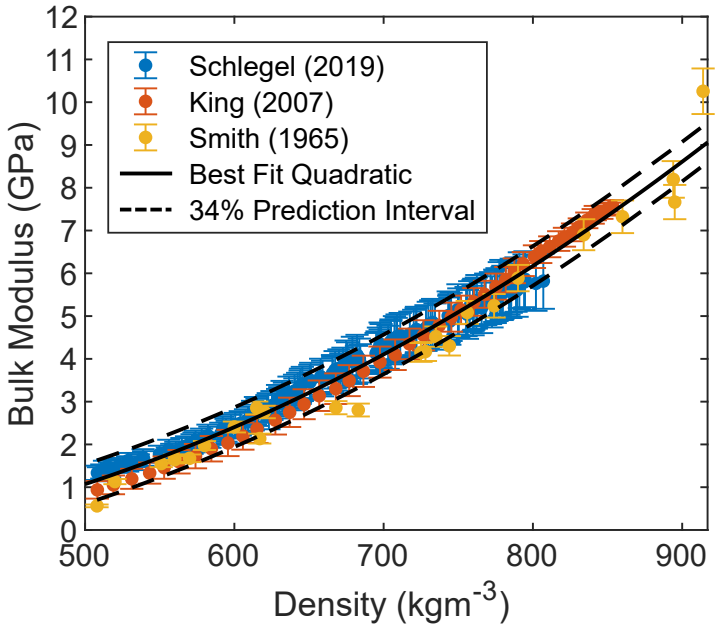

Figure S5: Data points and best fit line approximating the relationship between firn density and firn bulk modulus.

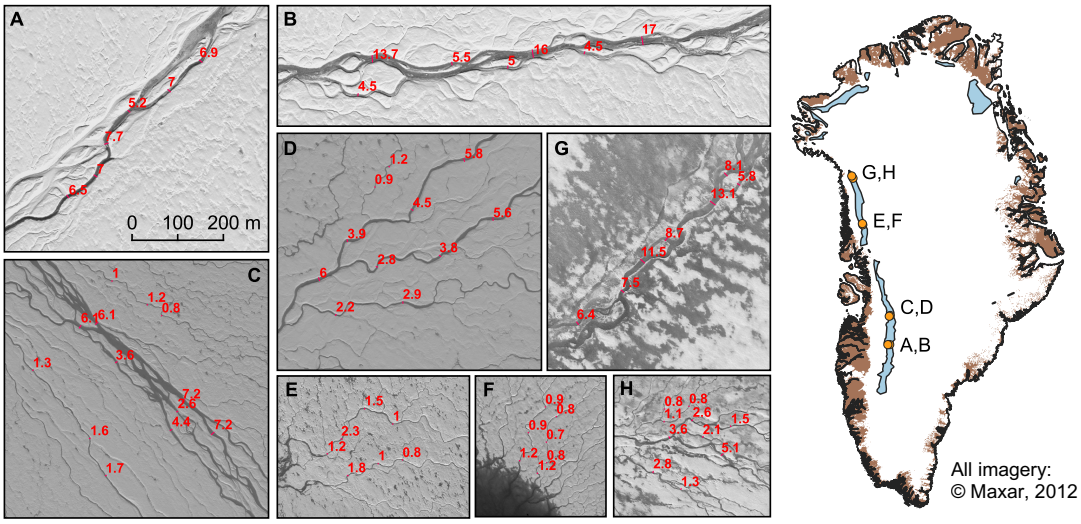

Figure S6: Selection of stream widths measured from panchromatic WorldView imagery over ice slab areas on Greenland's west coast in summer 2012. With widths ranging from 0.7 to 17 m, these data suggest that observed stream widths in these regions are broadly consistent with the small end of streams measured in the field in Smith et al. (2015).

Meng Y, Li W and Juanes R (2023) Crossover from viscous fingering to fracturing in cohesive wet granular media: a photoporomechanics study. *Soft Matter*, **19**(37), 7136–7148 (doi: 10.1039/D3SM00897E)